Comparative Analysis of Structural and Morphological Properties of Large-Pore Periodic Mesoporous Organosilicas and Pure Silicas

Xiao Ying Bao,[†] X. S. Zhao,*,[†] S. Z. Qiao,[‡] and S. K. Bhatia[‡]

Department of Chemical and Biomolecular Engineering, National University of Singapore,
10 Kent Ridge Crescent, Singapore 119620, and Department of Chemical Engineering,
The University of Queensland, Brisbane QLD 4072, Australia

A systematic study on the structural properties and external morphologies of large-pore mesoporous organosilicas synthesized using triblock copolymer $EO_{20}PO_{70}EO_{20}$ as a template under low-acid conditions was carried out. By employing the characterization techniques of SAXS, FE-SEM, and physical adsorption of N_2 in combination with α_s-plot method, the structural properties and external morphologies of large-pore mesoporous organosilicas were critically examined and compared with that of their pure-silica counterparts synthesized under similar conditions. It has been observed that unlike mesoporous pure silicas, the structural and morphological properties of mesoporous organosilicas are highly acid-sensitive. High-quality mesoporous organosilicas can only be obtained from synthesis gels with the molar ratios of HCl/H_2O between 7.08×10^{-4} and 6.33×10^{-3}, whereas mesoporous pure silicas with well-ordered structure can be obtained in a wider range of acid concentration. Simply by adjusting the HCl/H_2O molar ratios, the micro-, meso-, and macroporosities of the organosilica materials can be finely tuned without obvious effect on their structural order. Such a behavior is closely related to their acid-controlled morphological evolution: from necklacelike fibers to cobweb-supported pearl-like particles and to nanosized particulates.

1. Introduction

Periodic mesoporous organosilicas[1−3] (PMOs) synthesized by sol−gel hydrolysis and condensation of bridged silsesquinoxanes $(RO)_3-Si-R'-Si-(RO)_3$ in the presence of surfactant micelles represent one of the most remarkable developments in the area of ordered mesoporous materials.[4] With sophisticated choice of organic functionalities R',[5] surfactant templates,[6,7] and synthetic conditions, a large spectrum of PMOs of various properties has been synthesized,[6−16] which may find applications in catalysis,[10,17−18] electrocatalysis,[19] wastewater treatment,[11] nanostructure templating,[20] and so forth.

With regard to applications where large molecules are to be processed such as separation and purification of proteins, large-pore PMO materials are desired. SBA-15,[21] which is synthesized under acidic conditions in the presence of triblock copolymer $EO_{20}PO_{70}EO_{20}$, represents such large-pore materials. However, the majority of the previous synthetic routes toward SBA-15 PMOs followed the initial synthetic strategy, namely, under relatively strong acidic conditions,[21] which was observed not to be workable for synthesis of high-quality PMO materials.[22−25] To improve the structural quality of SBA-15 PMOs, special synthetic techniques such as true liquid crystal templating,[26] salt-assisted synthesis,[27] and solvent-assisted synthesis[28] have been explored. Instead of using these special synthetic techniques, we have recently developed a low-acid-concentration synthetic strategy for synthesis of highly ordered ethylene-bridged SBA-15 materials, and the critical role that acid (HCl) plays in the formation of ethylene-bridged large-pore organosilicas has been identified.[14] Our method does not involve any

salt additives or auxiliary solvents while affords highly ordered mesoporous PMOs.

Despite the wide interests in the synthesis of large-pore PMO materials, the structural and morphological properties of SBA-15 PMOs had hardly been characterized, yet these properties are important in terms of both fundamentals[29−31] and practical applications in catalysis,[32] bioimmobilization,[33] nanostructure templating,[34] and cosmetics.[35] In this study, we investigated the evolution of the structural and morphological properties of SBA-15 PMOs synthesized under low-acid conditions.[14] On the basis of the adsorption data of N_2, α_s-plot method[36] was employed to generate important structural parameters such as micro-, meso-, and macroporosity. Field-emission scanning electron microscopy (FE-SEM) was used to investigate the morphology of the materials prepared under different synthesis conditions. A relationship between the porous properties and particle morphologies was examined. Effort was also made to compare the differences of structural properties between SBA-15 PMOs and SBA-15 periodic mesoporous silicas (PMSs)[21] synthesized under similar conditions.

2. Experimental Section

2.1. Chemicals and Synthesis. 1,2-Bis(trimethoxysilyl)ethane (BTMSE, 96%, Aldrich), tetraethyl orthosilicate (TEOS, 98%, Fisher), triblock copolymer $EO_{20}PO_{70}EO_{20}$ (Pluronic P123, Aldrich), fuming hydrochloric acid (HCl, 37%, Merck), and absolute ethanol (99.98%, Merck) were used as received.

The syntheses of SBA-15 PMOs and PMSs were described previously by using BTMSE and TEOS as the organosilica and silica sources.[14] A series of samples were prepared by varying the amount of HCl added to the synthesis gels while keeping the amounts of other reactants constant. The SBA-15 PMO samples thus prepared are denoted as MSE*y*, where MSE

* To whom correspondence should be addressed. E-mail: chezxs@nus.edu.sg.
† National University of Singapore.
‡ The University of Queensland.

TABLE 1: Molar Compositions for Synthesizing MSE*y* and OS*y* Materials

sample	Si	P123	HCl	H_2O	HCl/H_2O	Si/P123
MSE1, OS1	1.00	0.0173	0.048	168	2.86×10^{-4}	58
MSE2, OS2	1.00	0.0173	0.119	168	7.08×10^{-4}	58
MSE3, OS3	1.00	0.0173	0.243	168	1.45×10^{-3}	58
MSE4, OS4	1.00	0.0173	0.490	168	2.92×10^{-3}	58
MSE5, OS5	1.00	0.0173	1.064	168	6.33×10^{-3}	58
MSE6, OS6	1.00	0.0173	3.773	168	2.25×10^{-2}	58
MSE4A	1.00	0.0138	0.490	168	2.92×10^{-3}	72
MSE	1.00	0	0.243	168	1.45×10^{-3}	

indicates organosilica precursor BTMSE, and *y*, ranging from 1 to 6, represents the molar ratios of HCl/H_2O in the synthesis gels, which were varied between 2.86×10^{-4} and 2.25×10^{-2}. The Si/P123 molar ratio used for the MSE*y* materials is 58. Precipitate was not observed within 1 day from the synthetic systems having HCl/H_2O molar ratios lower than 2.86×10^{-4}. After hydrothermal treatment at 100 °C for 5 days, the white solids were filtered, washed with copious water, and then dried under ambient conditions.

Keeping the other reaction parameters same as that used for MSE4 but increasing the Si/P123 ratio from 58 to 72, an SBA-15 PMO sample designated as MSE4A was obtained by reducing the amount of P123 used for synthesis. An organosilica sample without ordered mesopores, designated as MSE, was also synthesized with $HCl/H_2O = 1.45 \times 10^{-3}$ without the P123 template.

SBA-15 PMSs were prepared using systematically varied acid concentrations as that of PMOs. The PMS samples obtained are designated as OS*y*, where OS denotes silica precursor TEOS, and *y* stands for the same meaning as that of MSE*y*. Two moles of TEOS were considered to be equivalent to one mole of BTMSE.

Template removal from the SBA-15 materials was carried out by ethanol extraction for the water-washed samples at 70 °C for 6 h for one time. To investigate the effectiveness of template removal by water washing and ethanol extraction, one of the samples was neither water-washed nor ethanol-extracted. The effectiveness of template removal by repetition of the ethanol extraction process was also examined. The synthesis molar compositions for the samples involved in this study are compiled in Table 1.

2.2. Characterization. Fourier transform infrared (FTIR) spectra were collected on a Bio-Rad FTS 135 with a resolution of 2 cm^{-1} in the wavelength range of 400–4000 cm^{-1} using KBr technique. Small-angle X-ray scattering (SAXS) measurements were performed on a Bruker NanoStar at 40 kV and 35 mA with Cu Kα radiation of wavelength $\lambda = 1.542$ Å. The distance between sample and detector was 1.1 m. The scattered intensities, plotted against the scattering angle 2θ, were integrated azimuthally from the scattering patterns made up of several concentric circles. N_2 adsorption/desorption isotherms were collected on a Micromeritics ASAP volumetric adsorption analyzer at 77 K. Samples were outgassed at 373 K overnight before measurements. Field-emission scanning electron microscopy (FE-SEM) images were obtained with a JEOL JSM-6700F microscope.

2.3. Calculation Methods. Unit cell parameter, a, was obtained as described previously.[14] BET specific surface area, S_{BET}, and the BET parameter, C_{BET}, were obtained from adsorption data in the relative pressure P/P_0 range of 0.15–0.26 as recommended by Gregg and Sing.[36] Total pore volume, V_t, was estimated from the amount of N_2 adsorbed at $P/P_0 = 0.99$. Ordered mesopores are referred to as primary mesopores,
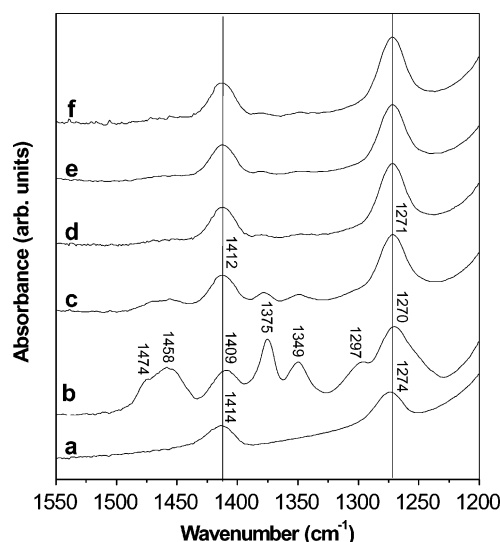

Figure 1. FTIR spectra of (a) MSE, (b) as-synthesized MSE3, (c) as-synthesized MSE3 after washing with copious water, (d) MSE3 after ethanol extraction one time, (e) MSE3 after ethanol extraction two times, and (f) MSE3 after ethanol extraction three times.

while pores with sizes equal or smaller than the ordered mesopores are considered as primary pores. The primary pore volume, V_p, and micropore volume, V_{mic}, were evaluated using the α_s-plot method.[36] The N_2 adsorption isotherm of a nonporous silica with a BET surface area of 26.2 m^2/g reported elsewhere[37] was used as the reference isotherm to construct α_s plots. Its validity for PMO materials has been demonstrated previously.[38] V_p was calculated in the ranges of $\alpha_s = 1.9$–2.9 for samples MSE1–MSE3, $\alpha_s = 2.3$–3.2 for samples MSE4 and MSE5, and $\alpha_s = 1.9$–2.4 for the OS*y* samples. V_{mic} was calculated in the range of 0.8–1.2 (P/P_0 from 0.2 to 0.58) for all samples. Primary mesopore volume, V_{mes}, was estimated from the difference between V_p and V_{mic}. Secondary pore volume, V_s, was obtained from the difference between V_t and V_p. Mesopore size distribution (PSD) curves were computed from the adsorption branches of the N_2 adsorption isotherms using the Barrett–Joyner–Halenda (BJH) algorithm. Primary mesopore size, w_d, was determined from the maximum of a PSD curve. Pore wall thickness, t, was assessed by subtracting w_d from a.

3. Results and Discussion

3.1. Template Removal. The removal of surfactant templates from PMOs is commonly carried out by means of alcohol-aided extraction[1–3,22,24,26,27] with or without the presence of acid. However, it has been reported that alcohol extraction may not be able to completely remove the surfactant templates.[2] The presence of trace surfactant template in PMO materials may affect their physical and surface properties, hence having influence on their adsorption properties. In this study, FTIR was used to monitor the degree of template removal for the SBA-15 PMOs.

Figure 1 shows the FTIR spectra of a representative PMO sample, MSE3, after different posttreatment stages, together with the amorphous organosilica sample MSE synthesized without surfactant P123. The absorption bands observed in the ranges of 1409–1414 cm^{-1} and 1270–1274 cm^{-1} are assigned to the bending vibrations of –CH$_2$– species in the ethylene bridges.[24] The intensities of these two bands were not affected upon ethanol extraction. These two bands are also observed on sample MSE (Figure 1a), and they are the only two bands observed on this sample in the wavenumber range of 1550–1200 cm^{-1}. The

Analysis of Organosilicas and Pure Silicas

J. Phys. Chem. B, Vol. 108, No. 42, 2004 **16443**

TABLE 2: Structural Parameters of the MSE*y* and OS*y* Materials Determined from their SAXS Patterns and N$_2$ Adsorption Isotherms
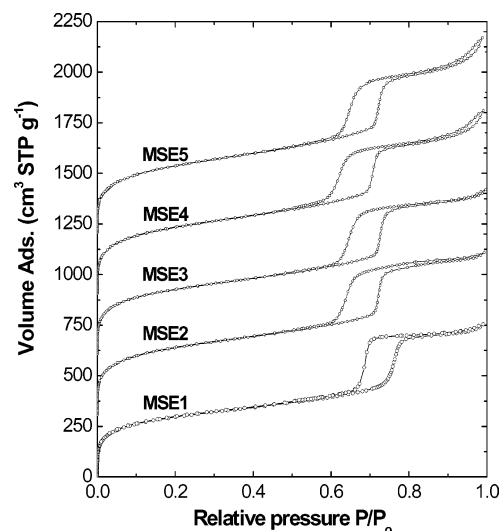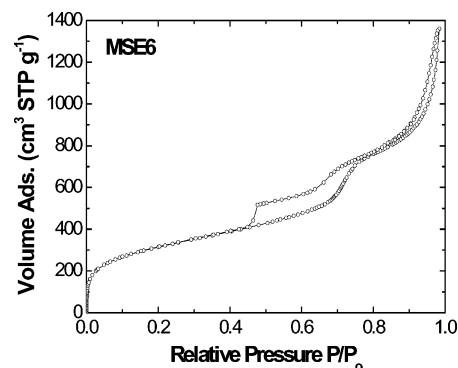
sample	a (nm)	S_{BET} (m^2/g)	C_{BET}	V_t (cm^3/g)	V_p (cm^3/g)	V_s (cm^3/g)	V_s/V_p	V_{mic} (cm^3/g)	V_{mes} (cm^3/g)	w_d (nm)	t (nm)
MSE1	12.91	964	−65	1.16	0.99	0.17	0.18	0.19	0.8	8.48	4.43
MSE2	12.59	1104	−70	1.24	1.10^a	0.14	0.13	0.21	0.89^a	7.34	5.25
MSE3	12.75	1067	−73	1.25	1.07^a	0.18	0.17	0.19	0.88^a	7.13	5.62
MSE4	12.44	1110	−108	1.40	0.95^b	0.45^c	0.47	0.18	0.77^b	6.71	5.73
MSE5	12.75	1130	−127	1.51	0.98^b	0.53^c	0.54	0.16	0.82^b	7.44	5.31
MSE6	12.59	1090	−1682	2.29	N.A^d	N.A^d	N.A^d	0.04	N.A^d	7.06	5.53
OS2	12.00	924	−141	1.24	1.06	0.17	0.16	0.10	0.96	7.57	4.43
OS5	13.08	698	755	1.18	0.95	0.23	0.24	0.01	0.94	8.71	4.37
OS6	12.75	838	252	1.48	0.19	0.29	0.24	0.00	1.19	9.14	3.64
MSE4A	12.59	1027	−68	1.09	0.96	0.13	0.14	0.20	0.76	6.66	5.93

^{a} The primary pore volumes V_p and the primary mesopores volume V_{mes} include the volumes of the type I pores. ^{b} The primary pore volumes V_p and the primary mesopore volumes V_{mes} include the volumes of type II pores. ^{c} The secondary pore volumes V_s do not include type II pores. ^{d} The primary pore volumes V_p, secondary pore volume V_s, and primary mesopore volume V_{mes} for material MSE6 could not be calculated using the α$_s$-plot method.[36]
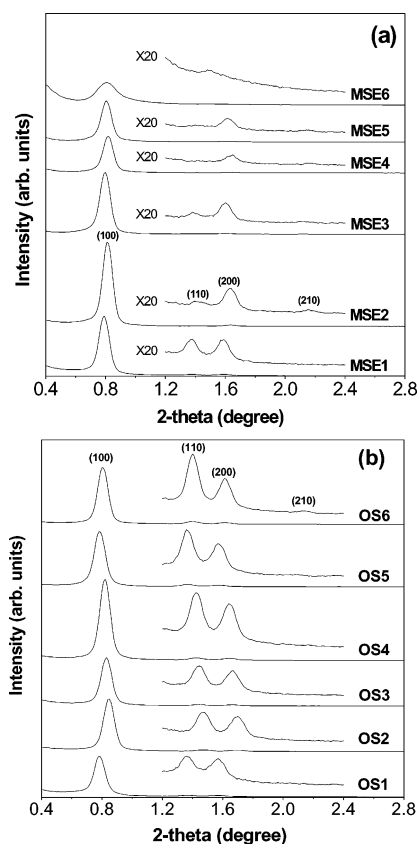
Figure 2. SAXS patterns of (a) MSE*y* and (b) OS*y* materials synthesized at various HCl/H$_2$O molar ratios.

Figure 3. N$_2$ adsorption/desorption isotherms of SBA-15 PMOs. The isotherms are offset vertically by 300, 600, 900, and 1200 cm^3 STP g^{-1} for samples MSE2, MSE3, MSE4, and MSE5, respectively.

Figure 4. N$_2$ adsorption/desorption isotherms of sample MSE6.

bands at 1474, 1458, 1375, 1349, and 1297 cm^{-1}, of which the intensities were decreased after water flushing and ethanol extraction, are attributed to the various deformation vibrations of the P123 template (Figure 1b−f). Water flushing of as-synthesized SBA-15 materials is able to remove a large fraction of the P123 template,[39] and this is verified by the sharp decrease in the deformation vibration intensities due to P123 template in the present study (Figure 1c). Ethanol extraction further reduced the amount of P123 template to a negligible level. Repeated extraction did not result in significant changes of the FTIR spectra (Figure 1e and f). Thus, it is believed that surfactant P123 had been essentially completely removed after one-time ethanol extraction.

3.2. Small-Angle X-ray Scattering. The SAXS patterns of the MSE*y* and OS*y* materials are displayed in Figure 2. The scattering peaks are indexed according to a 2D hexagonal symmetry (space group: *P6mm*). Highly ordered PMOs with sharp (100) peaks and higher order peaks were only formed at HCl/H$_2$O ratios less than 6.33×10^{-3}, while highly ordered PMSs were formed at all acid concentrations investigated. The unit cell parameters of the PMOs and PMSs are summarized in Table 2.

3.3. N$_2$ Adsorption/Desorption Isotherms. The N$_2$ adsorption/desorption isotherms of materials MSE1−MSE5 are shown in Figure 3 while the isotherms of sample MSE6 is depicted in Figure 4. The BJH PSD curves of the MSE*y* materials from the adsorption branches of the isotherms are shown in Figure 5. The BET surface areas, total pore volumes, primary mesopore sizes, and pore wall thicknesses are tabulated in Table 2.
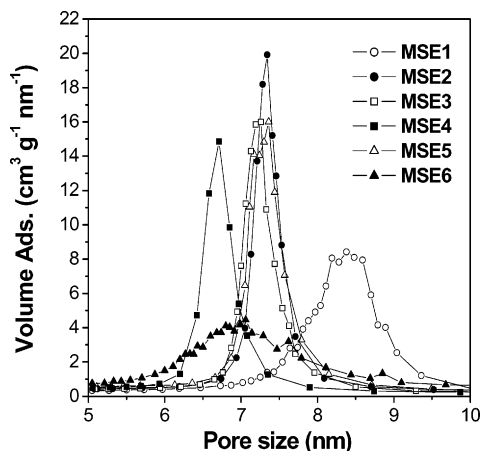
Figure 5. Pore size distributions for the SBA-15 PMOs.

A sharp capillary condensation step, demonstrating the presence of uniform mesopores, is seen from the isotherms of samples MSE1−MSE5. Compared with the isotherms of samples MSE2−MSE5, the capillary condensation steps of samples MSE1 and MSE6, especially of MSE6, are less pronounced, indicating a less ordered mesoporous structure. Corresponding to its comparatively sluggish capillary condensation, a relatively broad pore size distribution is seen on sample MSE1 synthesized with HCl/H$_2$O = 2.86 × 10^{-4}. Material MSE6 synthesized with HCl/H$_2$O = 2.25 × 10^{-2} also exhibits a broad pore size distribution, which is in agreement with its broad SAXS pattern (Figure 2a). The above observations further confirm the previous conclusion that highly ordered SBA-15 PMOs can only be obtained under controlled acid concentrations.[14]

With increasing acid concentrations of their synthesis gels, the pore sizes of samples MSE1−MSE4 were decreased from 8.48 to 6.71 nm with the most prominent pore size decrease occurring from sample MSE1 to sample MSE2 (from 8.48 to 7.34 nm). However, further increasing acid concentrations resulted in pore size increasing from 6.71 nm for sample MSE4 to 7.44 nm for sample MSE5. Sample MSE4, on the other hand, has the thickest pore wall (5.73 nm) among the MSE samples.

All MSEy materials exhibit a large S_{BET} value around 1000 m^2/g, indicating the formation of highly porous structures. The values of V_t were decreased monotonically with decreasing acid concentration from 2.29 cm^3/g for MSE6 to 1.16 cm^3/g for MSE1.

The sharp rises in the amount of nitrogen adsorbed at the low relative pressure region for samples MSE1−MSE6 strongly suggest the presence of micropores, which can be confirmed by their negative C_{BET} values as has been confirmed for PMS materials.[40] The C_{BET} parameter can be obtained from the BET equation,

$$\frac{z}{V(1-z)} = \frac{1}{C_{BET}V_m} + z\frac{(C_{BET}-1)}{C_{BET}V_m}$$

where $z = P/P_0$, V is the volume adsorbed at relative pressure z, V_m is the volume of monolayer adsorption, and C_{BET} is the BET parameter. Assuming a perfect linear fit so that C_{BET} is a constant over the relative pressure range used for S_{BET} analysis ($P/P_0 = 0.15−0.26$) and rearranging the BET equation yields

$$C_{BET} = \frac{(1-z)^2}{z\left[\left(\dfrac{V_m}{V}-1\right)+z\right]}$$

Thus, in the presence of micropores in a mesoporous sample, a substantial increase in the volume of N$_2$ adsorbed at the low relative pressure region will occur because of the micropore filling effect.[36] This increase will lead item [$(V_m/V) − 1 + z$] in the above equation to change from a positive value to zero, then to a negative value with increasing the amount of micropores presented in a sample. The values of C_{BET}, being inversely proportional to [$(V_m/V) − 1 + z$], will increase to an infinite positive value, pass through a discontinuity, be an infinite negative value, and then increase (but its absolute value will decrease) with increasing the amount of micropores presented in the mesoporous sample.[40]

The data in Table 2 show that the C_{BET} values for materials MSE1−MSE3 are comparable. However, the values of C_{BET} become more and more negative from sample MSE3 to sample MSE5, and finally to a very negative value for sample MSE6 (−1682). According to the above discussion of the relationship of C_{BET} with micropores, the changes of the C_{BET} values of samples MSE1−MSE6 indicate that the micropore volumes of samples MSE1−MSE3 are comparable, gradually decrease from samples MSE3 to MSE5, and sharply drop to a small value for sample MSE6.[36,40−42] These estimations are in good agreement with the values of V_{mic} calculated from the α$_s$-plot method (see Table 2).

One of the most prominent features of the isotherms shown in Figures 3 and 4 is the pronounced second hysteresis loops observed at the relative pressures above 0.85 for samples MSE4−MSE6 synthesized at relatively high-acid concentrations. The extent of the second hystereses decreases from sample MSE6 to sample MSE4, and it becomes insignificant for samples MSE3−MSE1. The presence of hysteresis loop at the high relative pressure region generally indicates the presence of secondary mesopores or macropores, which is usually attributed to the voids between the primary particles constituting the main bulk phase.[29] In addition, the isotherms of MSE2 feature a distinctively prominent primary hysteresis, which spans to the relative pressure of about 0.9. This could be due to the presence of a large amount of mesopores with sizes slightly above those of the primary mesopores. The nature of these mesopores in sample MSE2, being primary or secondary, will be discussed later.

For comparison purposes, the N$_2$ adsorption/desorption isotherms of representative SBA-15 PMSs synthesized at different acid concentrations are plotted in Figure 6. The BET surface areas, total pore volumes, primary mesopore sizes, and pore wall thicknesses calculated from the isotherms are included in Table 2. It is seen that the isotherms of the OSy materials resemble those of the highly ordered SBA-15 PMSs reported in the literature.[39,43] Unlike the earlier observations on SBA-15 PMOs synthesized in this study, the pore sizes of the SBA-15 PMSs were increased with increasing acid concentration. On the other hand, the pore wall thicknesses of the materials were decreased with increasing acid concentration. The second hysteresis seen on MSE4−MSE6 and the primary hysteresis spanning to high relative pressures seen on MSE2 are hardly observable on the SBA-15 PMSs synthesized with similar acid concentrations. The C_{BET} value is negative for OS2 (−141), and it becomes highly positive for OS5 (755) and then falls to 252 for OS6. This discontinuity of C_{BET} from a negative value to an exceptionally high, and then to a decreased positive value shows that the micropore volumes of SBA-15 PMSs also decrease with increasing acid concentration.[40] In addition, the S_{BET} values of SBA-15 PMSs are smaller than those of SBA-
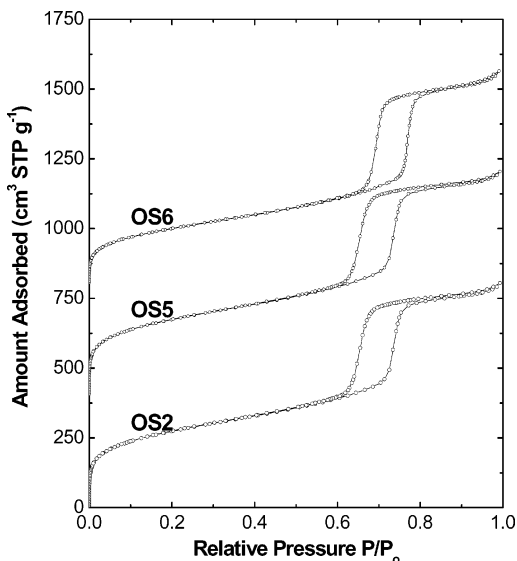
Analysis of Organosilicas and Pure Silicas

J. Phys. Chem. B, Vol. 108, No. 42, 2004 **16445**

Figure 6. N_2 adsorption/desorption isotherms of representative SBA-15 PMSs. The isotherms are offset vertically by 400 and 800 cm^3 STP g^{-1} for samples OS5 and OS6, respectively.

15 PMOs (698−924 cm^2/g), partially because of the lower bulk density of organosilica than pure silica.

3.4. Analysis with α_s-Plot Method and Field Emission SEM (FE-SEM). High-resolution α_s-plots of the SBA-15 PMOs calculated from their N_2 adsorption data are displayed in Figure 7. Using the α_s-plot of MSE5 (Figure 7e) as an example, four distinct stages can be identified.

Stage A represents a micropore filling process as revealed by the downward deviation of the α_s-plot from linearity. SBA-15 materials possess micropores.[39,43,44] The micropores, distributed in a corona around the primary mesopores, originate from the removal of the occluded PEO chains within the silica walls.[45−48] The absence of any appreciable steps in this stage indicates a broad micropore size distribution. The micropore volumes of the MSEy materials, calculated using the standard reduced adsorption α_s from 0.8 to 1.2 (P/P_0 from 0.2 to 0.58), are reported in Table 2. A gradual decrease in microporous volume from ∼0.20 cm^3/g for materials MSE1−MSE3 to 0.16 cm^3/g for MSE5 followed by a sharp decrease from 0.16 cm^3/g for MSE5 to 0.04 cm^3/g for MSE6 are seen, which agrees with the early discussion based on C_{BET} values.

Stage B is a multilayer adsorption process. The excellent linearity of the α_s-plots at this stage ($R^2 > 0.999$) for all the MSEy materials suggests a close similarity of the surface properties between the standard reference sample (a nonporous silica) and the SBA-15 PMOs in terms of N_2 adsorbate.[29] In fact, the α_s-plots of SBA-15 PMOs at stage A and B are highly similar to those of SBA-15 PMSs,[39,43] although the enhanced surface hydrophobicity brought about by ethylene bridges may weaken the interactions between N_2 adsorbate and the PMO surfaces.[38]

Stage C is a capillary condensation process in primary mesopores. The sharpness of this stage suggests the uniformity of the hexagonally arranged cylindrical mesopores. Different from materials MSE1−MSE5, material MSE6 exhibits an α_s-plot with a poorly defined stage C, which is in agreement with its broader pore size distribution curve.

Stage D is due to the adsorption on the external surfaces or in pores larger than the primary mesopores. Stage D is linear on MCM-41[49,50] and SBA-15 PMS materials.[39,43] However, a downward deviation from linearity is clearly seen for the initial part of stage D. Such deviation is not obvious for MSE1, but it

becomes prominent for sample MSE2 and MSE3, especially for sample MSE2 in the standard adsorption range of 1.5−1.8. Compared with that of samples MSE2 and MSE3, the downward deviations of samples MSE4 and MSE5 are mild, but extending to higher standard adsorption values (∼2.3). This downward deviation for MSE2−MSE5 is followed by a linear region at even higher standard adsorption values. For some materials such as MSE3, a slight upswing of the last point in its α_s-plot is seen, which is due to the condensation of N_2 at the pressures close to its saturation pressure P_0. In addition, the linear regions of stage D observed on other materials are not pronounced on sample MSE6.

The downward deviations seen at the initial parts of stage D for materials MSE2−MSE5 suggest the occurring of gas condensation in the relative pressure region. The deviations of MSE2 and MSE3 occurred at narrower standard adsorption ranges (α_s ranging from 1.5 to 1.8, corresponding to the pore sizes ranging from about 9 to 15 nm) than those of samples MSE4 and MSE5 (α_s ranging from 1.5 to 2.3, corresponding to the pore sizes ranging from about 9 to 45 nm), but steeper. These deviations could be a consequence of N_2 condensation in the pores that are larger than the primary mesopores but smaller than 200 nm, as no N_2 condensation occurs below the saturation pressure of N_2 when the pore size is greater than 200 nm.[29] The nature of these pores can be (1) ill-defined primary mesopores with sizes larger than the ordered primary mesopores (hereafter, type I pore), (2) secondary meso-macropores with sizes smaller than 200 nm[29] (hereafter, type II pore), or a combination of both. In reality, the pore size of either type I or type II pores is unlikely to be larger than 45 nm for nitrogen condensation to occur at α_s values below 2.3.

The linear section seen at the high α_s part of stage D ($\alpha_s > 1.8$ for MSE2 and MSE3 and $\alpha_s > 2.3$ for MSE4 and MSE5) implies a layer-by-layer adsorption mechanism on the external surfaces or on the surfaces of secondary macropores with a pore size greater than 200 nm[29] (hereafter, type III pore) wherein condensation would not occur at relative pressure ranges below the saturation pressure of N_2. The gradient of these linear segments, which is proportional to the surface areas of the type III pores and external surfaces, increases with increasing acid used for synthesis. This implies an increased amount of type III pores and external surface areas with increasing acid used for synthesis, probably because of reduced particle sizes or increased surface corrugations.

Different from MSE2 to MSE5, the stage D for MSE1 is totally linearizable, and the aforementioned downward deviation at stage D is not obvious for MSE1. Therefore, it is believed that material MSE1 is a simpler combination of ordered primary mesopores, type III pores, and external surfaces. The absence of a linear region in stage D for MSE6 suggests that the capillary condensation in secondary porosity occurs during the whole relative pressure ranges in stage D, which is an indication of an extremely broad secondary pore size distribution.

Figure 8 shows the α_s-plots of SBA-15 PMSs materials. A comparison of Figure 7 with Figure 8 reveals two differences. First, the downward deviation of stage A for SBA-15 PMSs is not as prominent as that of SBA-15 PMOs, especially for those SBA-15 PMSs synthesized under high-acid concentrations. The α_s-plot of OS6 synthesized at the highest acid concentration, for example, passes through the origin and shows a good linearity ($R^2 = 0.9998$) at the low-pressure range. Such linearity has been previously deemed as evidence supporting the absence of micropores in SBA-15 materials,[46] but its validity has recently been questioned.[41−42,54−55] Nevertheless, on a comparative basis,
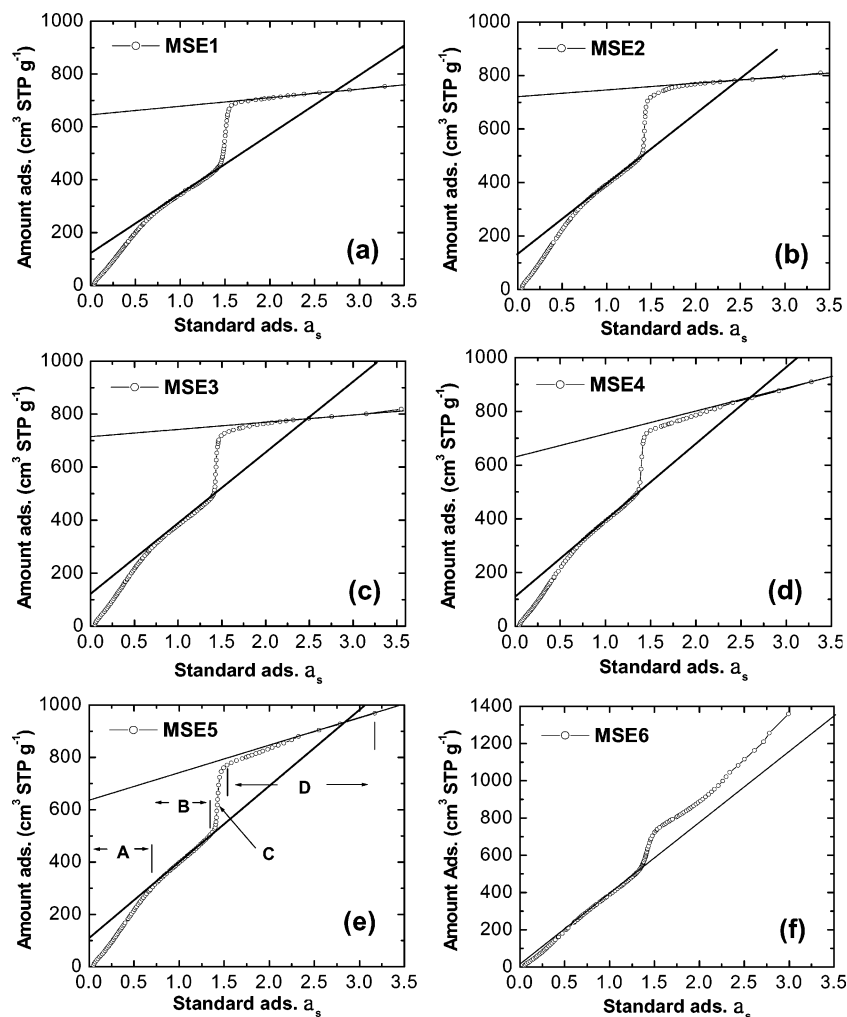
Figure 7. High-resolution α_s-plots of MSE materials.

it is safe to conclude that the SBA-15 PMOs synthesized in this work possess much larger micropore volumes than that of the SBA-15 PMSs synthesized under similar conditions. This may suggest that the PEO blocks of template P123 is able to penetrate into the PMO framework deeper than into the PMS framework.

Another difference between the α_s-plots of SBA-15 PMOs and SBA-15 PMSs is the absence of obvious downward deviations and the milder linear sections in stage D of the SBA-15 PMSs. The absence of downward deviation in PMSs is an indication of the absence of large quantities of type I and type II pores, while the mild linear sections show that the surface area of the type III pores and external surface areas in SBA-15 PMSs are also small compared with that of SBA-15 PMOs synthesized at high-acid concentrations, for example, materials MSE4 and MSE5. The above discussion can be further supported by the FE-SEM data presented below.

To account for the different adsorption properties between SBA-15 PMOs and SBA-15 PMSs and to investigate the secondary porosity of the SBA-15 PMOs, the particle morphologies of the materials were investigated by using FE-SEM and are shown in Figures 9 and 10. For SBA-15 PMOs, ropelike macrostructures with a length of around 100 μm and a diameter of less than 5 μm are predominant except for sample MSE6. Under higher magnifications, it is clearly seen that the ropelike morphologies are made up of bundles of parallel running necklace-shaped fibers for materials MSE1−MSE3. The neck-to-knot diameter ratio of each individual fiber of sample MSE1

is about 0.8. The morphologies of samples MSE2 and MSE3 are similar to that of MSE1 with slightly reduced diameters of both the knots and the necks of the necklace-shaped fibers. However, it seems that the diameter of the necks decreased faster than that of the knots as the acid concentration in the synthesis gels was increased. For example, the neck-to-knot diameter ratio of sample MSE3 is about 0.5, which is smaller than that of sample MSE1. Since particles with a smooth surface and an appreciable size in the micron range are seen on samples MSE1−MSE3, the presence of a large amount of type II pores, that is, secondary meso-macropores with sizes smaller than 200 nm, in these materials is unlikely. Thus, the deviations of the α_s-plots from linearity at the initial parts of stage D for samples MSE2 and MSE3 could be due to N_2 condensation in type I pores, that is, ill-defined primary mesopores, instead of type II pores. The increase of such type I pores at low-acid concentrations could be related to the sudden pore size expansion from MSE2 to MSE1, which is hence more prominent for MSE2 and MSE3, although the presence of them in MSE4 and MSE5 could not be precluded.

When the amount of acid in the synthetic system was further increased (samples MSE4 and MSE5, corresponding to the FE-SEM images shown in Figure 9d and e), the necks of the fibers are no longer seen. Instead, the fibers are made up of aligned near-spherical pearl-like particles or short cylindrical particles with a mean diameter of about 0.4 μm. Compared with sample MSE4, more short cylindrical particles are seen on sample MSE5, and the particles in MSE5 are slightly smaller. From
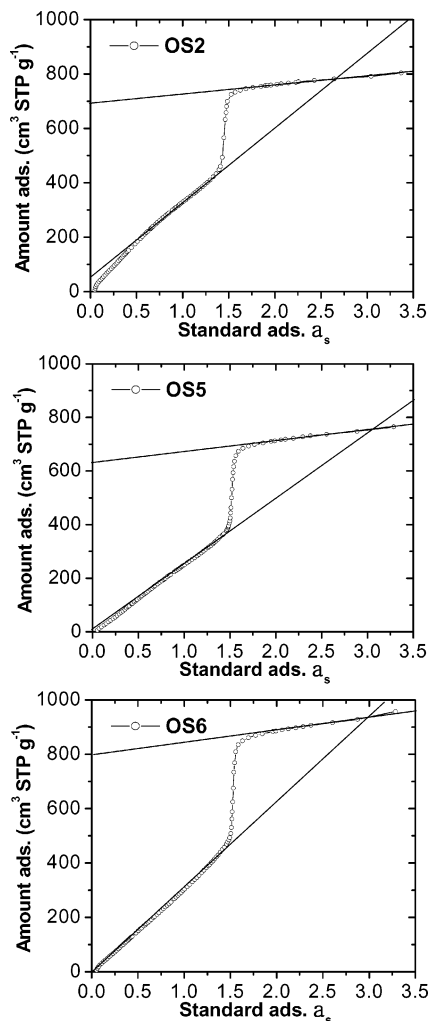
Analysis of Organosilicas and Pure Silicas

J. Phys. Chem. B, Vol. 108, No. 42, 2004 **16447**

Figure 8. High-resolution α_s-plots of PMS materials.

the images taken with a higher magnification (Figure 9g and h), it is seen that the surface of the pearl-like or short cylindrical particles are more corrugated in comparison with that of samples MSE1−MSE3. In addition, the particles in MSE4 are interconnected by many nanofibers, not only between neighboring particles from the same fiber, but also between particles of adjacent fibers. The presence of nanofibers is even more prominent in sample MSE5. The nature of the fibers, being hollow or solid, is currently under investigation. The diameters of the nanofibers are about several tens of nanometers. The quantity of the nanofibers is so large that they form a cobweblike network, which intervenes and splits the space between the interstitials of the primary particles into a large number of smaller spaces.

By reducing the amount of P123 used for synthesis and keeping all other synthesis parameters the same as MSE4,[51] we have prepared another highly ordered ethylene-bridged SBA-15 PMO (designed as MSE4A), which displays a ropelike morphology built from primary particles similar to that of samples MSE4 and MSE5, but without the presence of nanofibers interconnecting the primary particles (see Figure 9i and j). Besides, the surfaces of the particles of sample MSE4A, unlike that of MSE4, are rather smooth. Compared with that of MSE4, α_s-plot analysis of sample MSE4A (Figure 11) hardly showed the presence of any type II pores. Also, the external surface area of this material is small, as indicated by the gentle linear section in stage D of its α_s-plot. Nevertheless, its V_{mes} (discussed later) and V_{mic} are comparable with that of sample

MSE4 (Table 2). This shows that instead of reduced particle sizes, the large amount of type II pores and the high external surface area observed on samples MSE4 and MSE5 are mainly a consequence of the space-splitting effect of the nanofibers linking the pearl-like particles and the corrugated surfaces.

Different from other materials, highly irregular morphologies, which are composed of randomly aggregated, nanosized platelets, rods and particulates are observed on sample MSE6 (see Figure 9f). This is in agreement with the presence of a large amount of secondary interparticle meso-macopores of a wide size distribution inferred from the N_2 sorption data discussed above.

Figure 10 shows the FE-SEM images of representative OSy samples. A variety of morphologies, mainly faceted rods based on elongated hexagonal prisms, are seen on sample OS2, which was synthesized at a relatively low-acid concentration. The surfaces of the rods are smooth. However, a close examination reveals parallel stripes running down the main axis, indicating a good alignment of the mesopore channels along the long axis of the hexagonal prism.[52] The faceted rods are highly curved, resulting from disclinations rotated along the transverse axis in the *ab*-plane of the hexagonal prism.[53] The morphologies of samples OS4 and OS6 synthesized at relatively high-acid concentrations, on the other hand, are characterized by ropelike macrostructures similar to that of samples MSE1−MSE5. However, unlike that of MSE1−MSE5, the ropelike macrostructures of samples OS4 and OS6 are made up of parallel running faceted fibers with a constant diameter comparable with the rod diameter of sample OS2. The average diameter of the rods of the OSy materials is about 0.8 μm, which is larger than that of any SBA-15 PMO materials investigated. Therefore, the presence of a large amount of type II pores in the PMS materials is unlikely. Such observations are in good agreement with their SAXS and N_2 adsorption data, which suggested the presence of highly ordered mesopore structures, small quantity of type III pores and external surface areas, and the absence of a large quantity of type II pores on any of the SBA-15 PMS samples.

Having elucidated the nature of the downward deviation seen in stage D of the α_s-plots of the PMO materials, the primary pore volumes (V_p) and secondary pore volumes (V_s) of the MSEy and OSy materials obtained from their α_s-plots are reported in Table 2. For materials MSE2 and MSE3, their linear regions at high-standard adsorptions were carefully selected to calculate the V_p. The V_p of MSE2 and MSE3 so estimated includes the volumes of type I pores, or the ill-defined primary mesopores. On the other hand, the values of V_p estimated for MSE4 and MSE5 by using their linear sections of stage D include the volumes of type II pores, or the secondary meso-macopores with sizes smaller than 200 nm. In other words, the V_s's of samples MSE4 and MSE5, estimated as a difference of the V_t and V_p, are smaller than the actual values since the volumes of type II pores are not included. For MSE6, accurate estimations of V_p and V_s using its α_s-plot are practically impossible because of the poor resolution of the α_s-plot.

V_{mes}, obtained by subtracting V_{mic} from V_p, is the highest for materials MSE3 and MSE4 synthesized at intermediate acid concentrations. By a similar reasoning, V_{mes} should be treated with the same caution as the V_p mentioned before. On the other hand, V_s decreases dramatically as a function of decreasing HCl/H_2O ratio. Although a quantitative calculation for sample MSE6 is difficult because of the vague definition of stage D on its α_s-plot, an estimation based on the N_2 sorption isotherms and the α_s-plot reveals that V_{mes} is the lowest while V_s is the highest for sample MSE6, because the adsorption amount of its
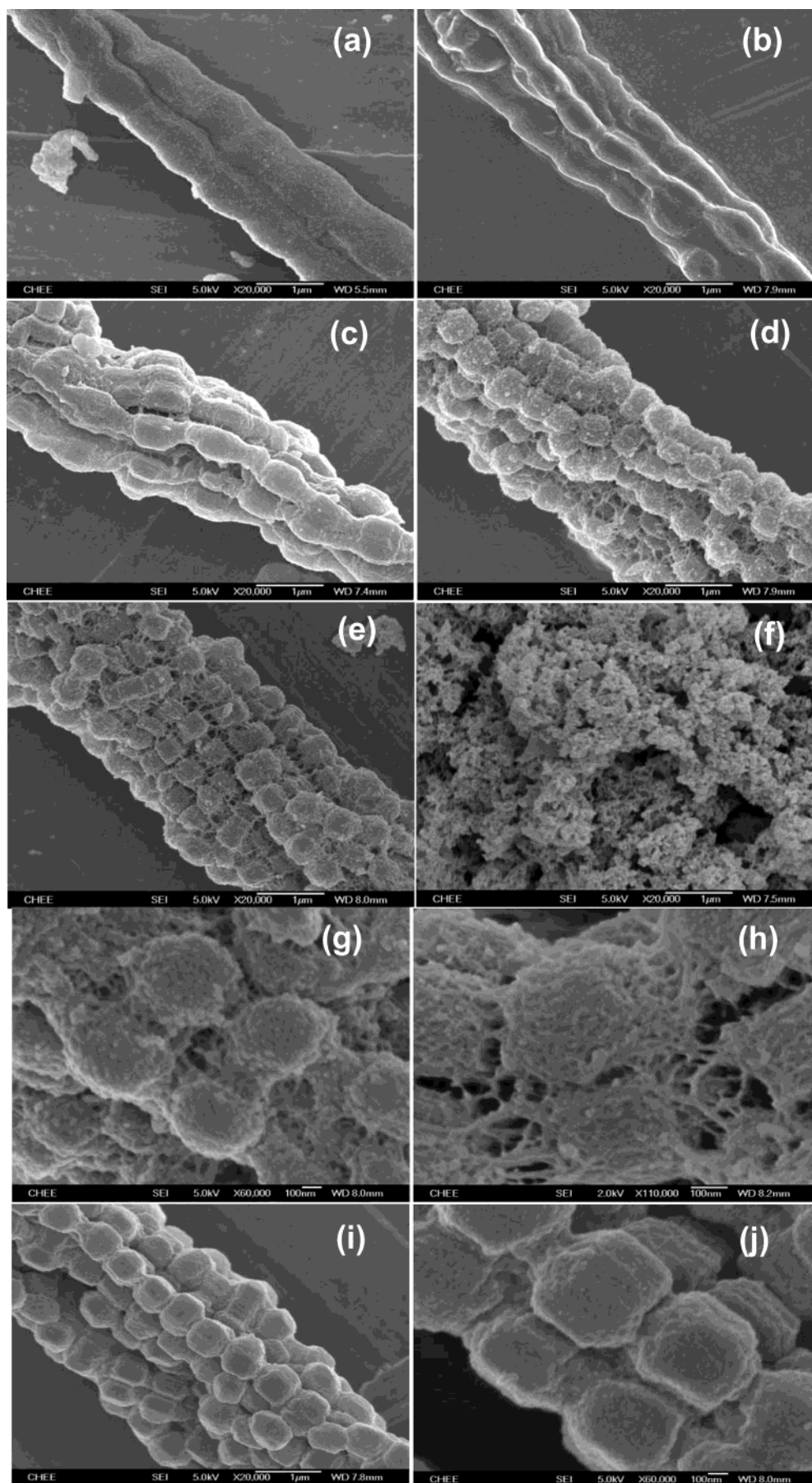
Figure 9. FE-SEM images of SBA-15 PMOs: (a) MSE1, (b) MSE2, (c) MSE3, (d) MSE4, (e) MSE5, (f) MSE6, (g) MSE4 of a larger magnification, (h) MSE5 of a larger magnification, (i) MSE4A, and (j) MSE4A of a larger magnification. The scale bars of images a−f and i are 1000 nm. The scale bars of images g, h, and j are 100 nm.
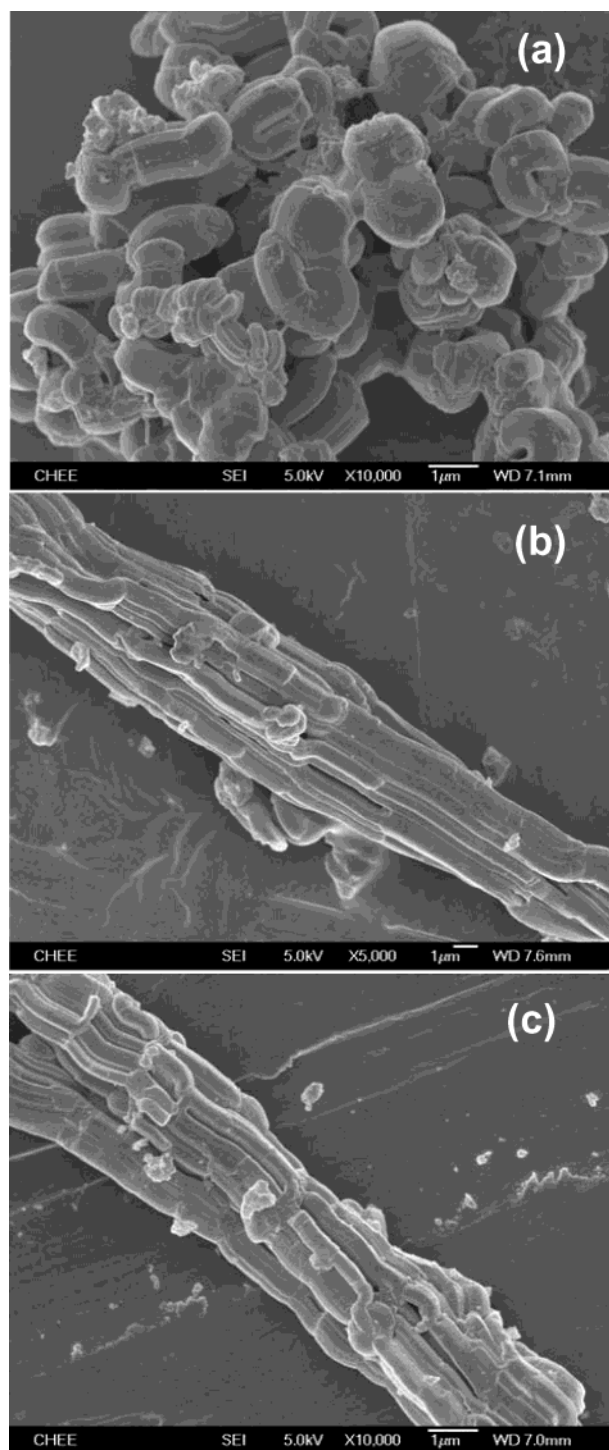
Analysis of Organosilicas and Pure Silicas

J. Phys. Chem. B, Vol. 108, No. 42, 2004 **16449**

Figure 10. FE-SEM images of representative SBA-15 PMSs: (a) OS2, (b) OS4, and (c) OS6. The scale bars are 1000 nm.

secondary hysteresis accounts for nearly half of the total adsorption amount.

Recently, the synthesis and characterization of mesoporous materials with secondary porosity or textural porosity have been largely explored.[32,56−60] The presence of hierarchically ordered, interconnecting pores of various sizes not only enhances accessibility of the active sites to reactant molecules[32,58] but also reduces transportation resistance in catalysis and adsorption.[32] However, previous efforts on synthesizing mesoporous materials with textural porosity usually involved additives or cumbersome synthesis procedures.[32,56−58] In addition, the scopes of their studies were mostly confined to small-pore materials such as M41S and MSU. Such studies on large-pore mesoporous
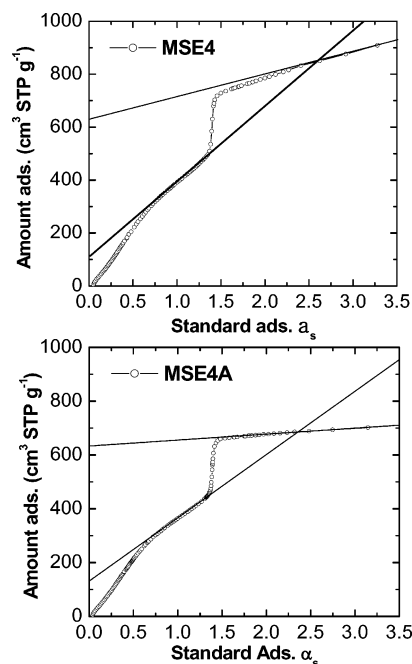

Figure 11. High-resolution α_s-plots of SBA-15 PMO samples MSE4 and MSE4A.

materials such as SBA-15 have hardly been available. The present study shows that the relative amount of secondary pore volume over primary pore volume V_s/V_p can be finely tuned from 0.10 to 0.54 and to an even larger value (e.g., for sample MSE6) by simply adjusting the amount of acid used in synthesis.

4. Conclusions

In this paper, the evolution of the porous properties and external morphologies of SBA-15 PMOs and SBA-15 PMSs under low-acid synthetic conditions has been comparatively characterized and critically examined. A relationship between the porous properties and particle morphologies has been established. Highly ordered SBA-15 PMOs with tunable pore sizes ranging from 6.7 to 8.5 nm have been synthesized. Unlike SBA-15 PMSs, it has been observed that SBA-15 PMOs with highly ordered pore structure can only be synthesized at relatively low-acid concentrations. The HCl/H_2O molar ratios used for synthesis have a drastic effect on the structural, texural, and morphological properties of the SBA-15 PMOs. It has also been observed that SBA-15 PMOs possess a larger fraction of microporosity than SBA-15 PMSs. Tuning of the secondary/primary porosities of SBA-15 PMOs can be easily achieved simply by varying the ratio of HCl/H_2O without affecting their structures. On the other hand, SBA-15 PMOs of different morphologies can be obtained by adjusting the acid concentration during synthesis. For example, the necklacelike fibers and the cobweb-supported pearls had never been observed previously for mesoporous silicas templated by surfactants. Furthermore, the cobweblike network splits the intersitial spaces of the pearl-like particles into numerous smaller spaces, which contribute to the tunability of the interparticle meso-macroporosity of the SBA-15 PMOs. The cobweblike network, together with the interparticle meso-macroporosity that it brings, can be easily tailored without affecting any other properties of the SBA-15 PMO simply by changing the synthetic recipe.

References and Notes

(1) Inagaki, S.; Guan, S.; Fukushima, Y.; Ohsuna, T.; Terasaki, O. *J. Am. Chem. Soc.* **1999**, *121*, 9611.

(2) Melde, B. J.; Holland, B. T.; Blanford, C. F.; Stein, A. *Chem. Mater.* **1999**, *11*, 3302.

(3) Asefa, T.; MacLachlan, M. J.; Coombs, N.; Ozin, G. A. *Nature* **1999**, *402*, 867.

(4) Beck, J. S.; Vartuli, J. C.; Roth, W. J.; Leonowicz, M. E.; Kresge, C. T.; Schmitt, K. D.; Chu, C. T-W.; Olson, D. H.; Sheppard, E. W.; McCullen, S. B.; Higgins, J. B.; Schlenker, J. L. *J. Am. Chem. Soc.* **1992**, *114*, 10834.

(5) Shea, K. J.; Loy, D. A. *Chem. Mater.* **2001**, *13*, 3306.

(6) Lee, B.; Luo, H. M.; Yuan, C. Y.; Lin, J. S.; Dai, S. *Chem. Commun.* **2004**, 240.

(7) Cho, E. B.; Char, K. *Chem. Mater.* **2004**, *16*, 270.

(8) MacLachlan, M. J.; Asefa, T.; Ozin, G. A. *Chem.—Eur. J.* **2000**, *6*, 2507.

(9) Asefa, T.; Yoshina-Ishii, C.; MacLachlan, M. J.; Ozin, G. A. *J. Mater. Chem.* **2000**, *10*, 1751.

(10) Baleizão, C.; Gigante, B.; Das, D.; Alvaro, M.; Garcia, H.; Corma, A. *Chem. Commun.* **2003**, 1860.

(11) Burleigh, M. C.; Jayasundera, S.; Spector, M. S.; Thomas, C. W.; Markowitz, M. A.; Gaber, B. P. *Chem. Mater.* **2004**, *16*, 3.

(12) Inagaki, S.; Guan, S.; Ohsuna, T.; Terasaki, O. *Nature* **2002**, *416*, 304.

(13) Guo, W. P.; Kim, I.; Ha, C. S. *Chem. Commun.* **2003**, 2692.

(14) Bao, X. Y.; Zhao, X. S.; Li, X.; Chia, P. A.; Li, J. *J. Phys. Chem. B* **2004**, *108*, 4684.

(15) Burleigh, M. C.; Markowitz, M. A.; Jayasundera, S.; Spector, M. S.; Thomas, C. W.; Gaber, B. P. *J. Phys. Chem. B* **2003**, *107*, 12628.

(16) Cerveau, G.; Corriu, R. J. P.; Lerouge, F.; Bellec, N.; Lorcy, D.; Nobili, M. *Chem. Commun.* **2004**, 396.

(17) Bhaumik, A.; Kapoor, M. P.; Inagaki, S. *Chem. Commun.* **2003**, 470.

(18) Kapoor, M. P.; Sinha, A. K.; Seelan, S.; Inagaki, S.; Tsubota, S.; Yoshida, H.; Haruta, M. *Chem. Commun.* **2002**, 2902.

(19) Doménech, A.; Alvaro, M.; Ferrer, B.; García, H. *J. Phys. Chem. B* **2003**, *107*, 12781.

(20) Sakamoto, Y.; Fukuoka, A.; Higuchi, T.; Shimomura, N.; Inagaki, S.; Ichikawa, M. *J. Phys. Chem. B* **2004**, *108*, 853.

(21) Zhao, D.; Huo, Q.; Feng, J.; Chmelka, B. F.; Stucky, G. D. *J. Am. Chem. Soc.* **1998**, *120*, 6024.

(22) Burleigh, M. C.; Markowitz, M. A.; Wong, E. M.; Lin, J. S.; Gaber, G. P. *Chem. Mater.* **2001**, *13*, 4411.

(23) Cho, E. B.; Kwon, K. W.; Char, K. *Chem. Mater.* **2001**, *13*, 3837.

(24) Muth, O.; Schellbach, C.; Fröba, M. *Chem. Commun.* **2001**, 2032.

(25) Matos, J. R.; Kruk, M.; Mercuri, L. P.; Jaroniec, M.; Asefa, T.; Coombs, N.; Ozin, G. A.; Kamiyama, T.; Terasaki, O. *Chem. Mater.* **2002**, *14*, 1903.

(26) Zhu, H. G.; Jones, D. J.; Zajac, J.; Roziere, J.; Dutartre, R. *Chem. Commun.* **2001**, 2568.

(27) Guo, W. P.; Park, J. Y.; Oh, M. O.; Jeong, H. W.; Cho, W. J.; Kim, I.; Ha, C. S. *Chem. Mater.* **2003**, *15*, 2295.

(28) Wang, W.; Xie, S.; Zhou, W.; Sayari, A. *Chem. Mater.* **2004**, *16*, 1756.

(29) Kruk, M.; Jaroniec, M. *Chem. Mater.* **2001**, *13*, 3169.

(30) Yang, H.; Coombs, N.; Ozin, G. A. *Nature* **1997**, *386*, 692.

(31) Lin, H. P.; Mou, C. Y. *Acc. Chem. Res.* **2002**, *35*, 927.

(32) Pauly T. R.; Liu Y.; Pinnavaia T. J.; Billinge S. J. L.; Rieker T. P. *J. Am. Chem. Soc.* **1999**, *121*, 8835.

(33) Fan, J.; Lei, J.; Wang, L. M.; Yu, C. Z.; Tu, B.; Zhao, D. Y. *Chem. Commun.* **2003**, 2140.

(34) Yu, C. Z.; Fan, J.; Tian, B. Z.; Zhao, D. Y.; Stucky, G. D. *Adv. Mater.* **2002**, *14*, 1742.

(35) Shio, S.; Kimura, A.; Yamaguchi, M.; Yoshida, K.; Kuroda, K. *Chem. Commun.* **1998**, 2461.

(36) Gregg, S. J.; Sing, K. S. W. *Adsorption, Surface Area and Porosity*; Academic Press: London, 1982.

(37) Jaroniec, M.; Kruk, M.; Olivier, J. P. *Langmuir* **1999**, *15*, 5410.

(38) Kruk, M.; Jaroniec, M.; Guan, S.; Inagaki, S. *J. Phys. Chem. B* **2001**, *105*, 681.

(39) Kruk, M.; Jaroniec, M.; Ko, C. H.; Ryoo, R. *Chem. Mater.* **2000**, *12*, 1961.

(40) Galarneau, A.; Cambon, H.; Di Renzo, F.; Fajula, F. *Langmuir* **2001**, *17*, 8328.

(41) Galarneau, A.; Cambon, H.; Di Renzo, F.; Ryoo, R.; Choi, M.; Fajula, F. *New J. Chem.* **2003**, *27*, 73.

(42) Nossov, A.; Haddad, E.; Guenneau, F.; Galarneau, A.; Di Renzo, F.; Fajula, F.; Gédéon, A. *J. Phys. Chem. B* **2003**, *107*, 12456.

(43) Ryoo, R.; Ko, C. H.; Kruk, M.; Antochshuk, V.; Jaroniec, M. *J. Phys. Chem. B* **2000**, *104*, 11465.

(44) Lukens, W. W., Jr.; Schmidt-Winkel, P.; Zhao, D.; Feng, J.; Stucky, G. D. *Langmuir* **1999**, *15*, 5403.

(45) Joo, S. H.; Ryoo, R.; Kruk, M.; Jaroniec, M. *J. Phys. Chem. B* **2002**, *106*, 4640.

(46) Impéror-Clerc, M.; Davidson, P.; Davidson, A. *J. Am. Chem. Soc.* **2000**, *122*, 11925.

(47) Ruthstein, S.; Frydman, V.; Kababya, S.; Landau, M.; Goldfarb, D. *J. Phys. Chem. B* **2003**, *107*, 1739.

(48) Melosh, N. A.; Lipic, P.; Bates, F. S.; Wudl, F.; Stucky, G. D.; Fredrickson, G. H.; Chmelka, B. F. *Macromolecules* **1999**, *32*, 4332.

(49) Zhu, H. Y.; Zhao X. S.; Lu, G. Q.; Do, D. D. *Langmuir* **1996**, *12*, 6513.

(50) Jaroniec, M.; Kruk, M.; Shin, H. J.; Ryoo, R.; Sakamoto, Y.; Terasaki, O. *Microporous Mesoporous Mater.* **2001**, *48*, 127.

(51) Bao, X. Y.; Zhao, X. S.; Li, J.; Li X. *Appl. Surf. Sci.* **2004**, *237*, 380.

(52) Kosuge, K.; Sato, T.; Kikukawa, N.; Takemori, M. *Chem. Mater.* **2004**, *16*, 899.

(53) Yang, H.; Ozin, G. A.; Kresge, C. T. *Adv. Mater.* **1998**, *10*, 883.

(54) Kruk, M.; Jaroniec, M. *Chem. Mater.* **2001**, *13*, 1726.

(55) Ravikovitch, P. I.; Neimark, A. V. *J. Phys. Chem. B* **2001**, *105*, 6817.

(56) Wang, X. Z.; Dou, T.; Xiao, Y. Z. *Chem. Commun.* **1998**, 1035.

(57) Sun, J. H.; Shan, Z. P.; Maschmeyer, T.; Moulijn, J. A.; Coppens, M. O. *Chem. Commun.* **2001**, *24*, 2670.

(58) Blanford, C. F.; Yan, H.; Schroden, R. C.; Al-Douas, M.; Stein, A. *Adv. Mater.* **2001**, *13*, 401.

(59) El Haskouri, J.; de Zárate, D. O.; Guillem, C.; LaTorre, J.; Caldés, M.; Beltrán, A.; Beltrán, D.; Descalzo, A. B.; Rodríguez-López, G.; Martínez-Mánez, R.; Marcos, M. D.; Amorós, P. *Chem. Commun.* **2002**, 330.

(60) Lee, J.; Kim, J.; Hyeon, T. *Chem. Commun.* **2003**, 138.